

Wind Erosion on Mars and other Small Terrestrial Planets

Maximilian Kruss, Grzegorz Musiolik, Tunahan Demirci¹, Gerhard Wurm¹, Jens Teiser

University of Duisburg-Essen, Faculty of Physics, Lotharstr. 1-21, 47057 Duisburg, Germany

Abstract

We carried out wind tunnel experiments on parabolic flights with 100 μm Mojave Mars simulant sand. The experiments result in shear stress thresholds and erosion rates for varying g -levels at 600 Pa pressure. Our data confirm former results on JSC Mars 1A simulant where the threshold shear stress is lower under Martian gravity than extrapolated from earlier ground-based studies which fits observations of Martian sand activity. The data are consistent with a model by Shao and Lu (2000) and can also be applied to other small terrestrial (exo)-planets with low pressure atmospheres.

Keywords: Mars, Saltation, Microgravity Experiments, Cohesion, Aeolian Processes

1. Introduction

Dust storms are a common phenomenon on Earth. They can e.g. be observed in the Sahara, which is the largest source of aeolian soil dust and sand on Earth (Schütz et al., 1981; Goudie and Middleton, 2001). The causes and consequences of dust storms cannot be attributed to simple mechanisms. The behavior on the global scale is chaotic and the frequency of such storms changes over time (Goudie and Middleton, 1992). However, conditions for dust and sand activity can be described with a microscopical force balance between gravity, cohesion, lifting wind forces and other attractive and repelling forces, e.g. a Coulomb force for single grains (Shao and Lu, 2000; Kok et al., 2012).

Beyond Earth, dust storms are observed on the Martian surface and have a huge impact on the planet's weather (Smith, 2004; Heavens et al., 2011; Zurek, 2017). However, aeolian particle transport on Mars is still not fully constrained as indicated by recent observations (Lapotre et al., 2016; Baker et al., 2018). The main difficulties researching dust storm activity on Mars are the altered gravity of $0.38 g_E$ with Earth's gravity $g_E = 9.81 \text{ m s}^{-2}$ and the low pressure of 6 mbar. Experiments at low pressure but $1 g_E$ were carried out in the past, e.g., in the Martian surface wind tunnel at NASA Ames (Greeley et al., 1976, 1980; Greeley and Iversen,

1985). Greeley et al. (1980) modelled the particle lifting in $0.38 g_E$ with low-density materials. However, the inferred wind velocities needed to mobilize grains were higher than wind speeds on Mars, e.g., measured by the Viking and Phoenix landers, and could not explain particle occurrence within the Martian atmosphere (Hess et al., 1977; Schofield et al., 1997; Forget et al., 1999; Holstein-Rathlou et al., 2010). White et al. (1987) studied the gravity dependence on the threshold wind speed for motion initiation with a centrifuge on a parabolic flight. However, their experiments were performed under Earth's atmospheric conditions. Despite all studies in the last decades, it is still an open question which mechanisms advantage particle lifting and how strongly they contribute to it (White et al., 1987; Sullivan et al., 2005; Greeley et al., 2006; Merrison et al., 2008; Sullivan et al., 2008; Kok, 2010b; Bridges et al., 2012). Durán et al. (2011) and Rasmussen et al. (2015) give comprehensive overviews on aeolian sediment transport and mass fluxes. Numerical simulations often use artificially reduced thresholds for motion initiation to match the observations (Daerden et al., 2015). Effects like thermal creep due to the illumination by the sun (de Beule et al., 2014), the pressure drops within dust devils (Ellehoj et al., 2010), a lowered sediment compression in lower gravity (Musiolik et al., 2018), or different materials might support particle lifting in general.

Until today, no studies of the particle lifting mechanism for a freely chosen (low) gravity and (low) pressure exist. This is certainly attributed to the lack of

Email address: maximilian.kruss@uni-due.de (Maximilian Kruss)

small terrestrial planets with atmospheres in the Solar System in which dust and sand activity is possible. However, the number of exoplanets detected over the last years is large and the data base is continuously growing (exoplanet.eu, 2019). Phase curves of planets or transit measurements might provide information on the surface or atmosphere of exoplanets. As planets like Mars can enshroud themselves in planet encircling dust storms, it is important to understand how particles are lifted under different gravity and different atmospheric conditions, i.e. pressure.

In this study, we significantly extend earlier work by Musiolik et al. (2018) who argue that threshold velocities needed to initiate saltation might not be as high as thought before. While that data pointed in a favorable direction, the amount of total data was rather scarce. We expand the database significantly here. Besides measurements of threshold velocities with another sample material, we also present data in a wider gravity range of $0.15 - 1 g_E$ and compare it to theoretical models. Furthermore, new aspects of erosion rates and gravity dependence are presented in this work for the first time.

2. Experiments

2.1. Microgravity Setup

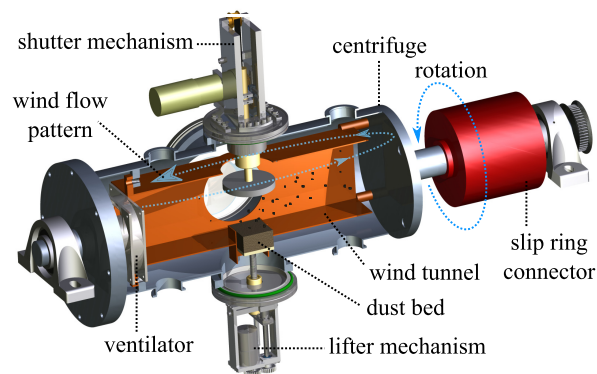


Figure 1: Schematic of the experiment from Musiolik et al. (2018).

The experimental setup is shown in Fig. 1 and is the same which was used by Musiolik et al. (2018) and Demirci et al. (2019). For details, the reader is referred to these studies. However, the principle of the experiment is summarized as follows. The setup consists of a low pressure wind tunnel with a cross-section of 10×10 cm which is mounted onto a centrifuge. The rotation speed determining the centrifugal forces can be set up to 2 Hz. As the experiments were carried out under microgravity conditions during a parabolic flight

with residual acceleration smaller than $0.05 g_E$, it was possible to simulate an acceleration between around 0.15 and $1 g_E$. The force was acting on a 4×4 cm sized sample bed which was exposed to the wind flow of an adjustable fan. The maximum wind speed in the centre of the wind tunnel is around 15 m s^{-1} . Within the scope of this work, the wind velocity in the centre of the wind tunnel is of minor importance, as the wind velocity is traced close to the surface of the sample bed. After passing the wind tunnel, the gas can flow back through the free space between the wind tunnel and the vacuum chamber, as it is illustrated in Fig. 1. The maximum Reynolds number inside the wind tunnel is on the order of $Re \approx 800$ but the exact wind profile is not known. Since it takes some time until a certain fan velocity is established wind speeds were not varied within a parabola but kept constant.

There are two additional mechanisms to control the sample bed. A shutter, which only opens for the measurements in microgravity, covers the sample to avoid any particle spillage. The lifter unit underneath the particle bed can push the sample up to ensure that the surface of the sample is always exposed to the wind.

Prior to the parabolic flight, the chamber was filled with CO_2 at a pressure of around 6 mbar which equals Martian atmospheric conditions. We note that the experiment was carried out under room temperature. Real temperatures on Mars are subject to large diurnal and seasonal variations as are pressures and it has to be kept in mind that local temperature but also pressure on Mars might differ from our experimental conditions. For each parabola a set of rotation frequency and wind speed was chosen. Potential erosion of the particle bed was observed from the side with a camera at a frame rate of 450 fps using bright field illumination. Camera and illumination are not shown in Fig. 1 for simplicity.

2.2. Sample

Mojave Mars Simulant (MMS), which is a common analog for Martian regolith (Peters et al., 2008), was used as sample for these experiments. Obviously, choosing a realistic material for different planetary surfaces in general is not possible. However, basaltic material seems to be appropriate since it is very abundant in the Solar System and we consider it as suitable for the designed experiment.

The sample was tempered at 200°C for 24 h to remove volatiles (especially water). It was then sieved to limit the range of grain sizes. The grain size distribution was determined using a commercial device (Mastersizer 3000, Malvern Instruments) based on light scattering.

The resulting grain size distribution (see Fig. 2) is bi-modal: There is a fraction of dust particles from around 1 to 15 μm . Noting the logarithmic scale, this is measurable but in total it is only a small contribution to the total particle volume. Besides this dust fraction there is a broad peak of sand grains around 100 μm in size. Only the sand is accessible for observations due to the limited spatial resolution of the camera. Like in Musiolik et al. (2018) the shutter lifts a large part of the sample every time it is opened. As the lifted particles fall back afterwards, the surface layers of the sample always consist of grains which settled under the respective low gravity.

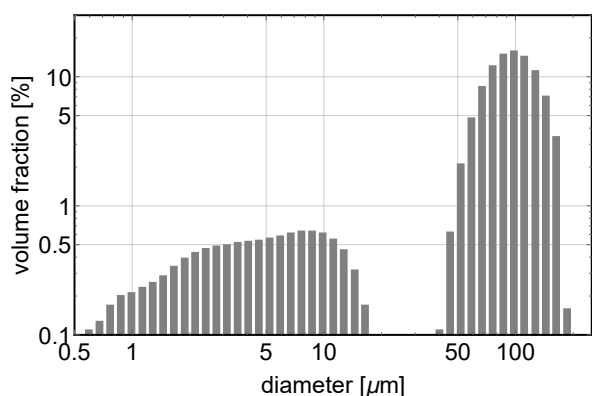


Figure 2: Grain size distribution of the used sample measured by a commercial device based on light scattering.

3. Results

3.1. Saltation Threshold

Once the wind-induced shear stress on the surface reaches a certain value, motion of individual grains is initiated. This threshold shear stress $\tau_t = \rho u_t^{*2}$ is characterized by the threshold friction velocity of the wind u_t^* and the gas density ρ . By varying the fan speed in the given setup, the threshold between particle motion and no motion can be observed. It has to be noted that the wind velocity can only be changed in discrete steps.

The applied friction velocity u_a^* at a given fan speed is determined by analyzing the trajectories of lifted grains. Fig. 3 shows an example trace of a lifted particle. This measurement was carried out slightly above the threshold of motion initiation. Wind speeds only lower by one discrete step did not affect the sample bed. Grains of the given size at the low pressure are not instantly coupled to the gas. They are accelerated during observation. The coupling process is characterized by a coupling time t_c . The acceleration of the grains in flow

direction (x -direction) at a constant height h above the sample bed is, e.g., described by Wurm et al. (2001)

$$x(t, h) = (v(h) - v_0)t_c \exp\left(-\frac{t}{t_c}\right) + v(h)t + x_0, \quad (1)$$

with fit parameters $v(h)$, v_0 , t_c and x_0 being the gas velocity, the initial velocity, the coupling time and a constant, respectively. The wind profile above the surface can be mapped by tracking several grains which are lifted to different heights. We did not restrict the analysis to a certain point of time or location, but considered lifting events over several seconds and along the whole sample bed. This way any temporary fluctuations are averaged.

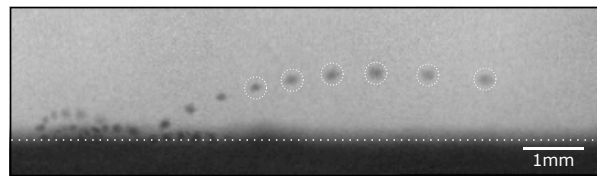


Figure 3: Superposition of 10 subsequent frames at the threshold under Martian gravity. The encircled positions of the lifted particle were used for the fit of the gas velocity according to Eq. 1. The dotted line indicates the surface of the particle bed ($h = 0$).

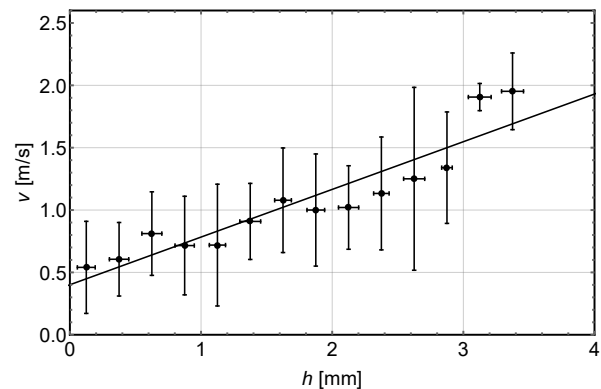


Figure 4: Wind velocity profile at the threshold under Martian gravity. Here, a total of more than 200 individual values were binned. The error bars show the standard deviations of all values in the respective intervals. The linear fit is described by $v(h) = (382 \pm 46) \text{ s}^{-1} \cdot h + (0.40 \pm 0.09) \text{ m s}^{-1}$.

As an example, Fig. 4 shows the wind profile at the threshold under Martian gravity. The variations of the binned data reflect the uncertainty of the size of lifted grains. It was not possible to determine their exact size based on the images. The resulting data was fitted linearly because in viscous sublayers close to the ground the velocity increase can be described as linear

with height (Sternberg, 1962). This dependence has also been applied in former work (Merrison et al., 2008; Musiolik et al., 2018; Demirci et al., 2019). The friction velocity in a Newtonian fluid is calculated according to (Schlichting and Gersten, 2006)

$$u^* = \sqrt{\frac{\eta}{\rho} \frac{dv(h)}{dh}}. \quad (2)$$

For CO₂ at room temperature and at a pressure of 6 mbar, the dynamic viscosity and the gas density are $\eta = 1.5 \times 10^{-5}$ Pa s (Laesecke and Muzny, 2017) and $\rho = 1.12 \times 10^{-2}$ kg m⁻³, respectively. This finally yields a measured threshold friction velocity for Martian gravity of $u_t^* = 0.72^{+0.04}_{-0.06}$ m s⁻¹. The uncertainty is calculated by error propagation taking into account the error of the slope in Fig. 4. In addition, the lower limit is also affected by the stepwise increase of the wind speed. The difference of u_a^* between two discrete steps is around 0.02 m s⁻¹. If the applied friction velocity exceeds u_t^* , the sand grains used in this experiment can be lifted under Martian conditions.

For extending the investigation from Mars to other planetary bodies and to get a better scaling on gravity in general, it is necessary to vary the gravitational forces acting on the sample bed. It was possible to determine the threshold friction velocities for five different accelerations, including a ground-based measurement. The results are summarized in Tab. 1. The uncertainty of the accelerations is caused by the residual accelerations during the parabolas.

Table 1: Threshold friction velocities at different gravitational accelerations.

gravity [m s ⁻²]	analyzed tracks	u^* [m s ⁻¹]
1.3 ± 0.5	127	0.55 ^{+0.04} _{-0.06}
2.5 ± 0.2	120	0.67 ^{+0.04} _{-0.06}
3.7 ± 0.2	208	0.72 ^{+0.04} _{-0.06}
5.7 ± 0.2	119	0.89 ^{+0.10} _{-0.12}
9.8	109	0.93 ^{+0.06} _{-0.08}

Shao and Lu (2000) developed an analytical expression for the dependence of u_t^* on gravity. In particular, they compare the shear stress necessary to lift a particle with the sum of gravity and cohesion, which has to be overcome:

$$\rho u_t^{*2} = A_N \left(\rho_p d g + \frac{\gamma}{d} \right). \quad (3)$$

The particle's density ρ_p , its diameter d and the gravitational acceleration g describe the influence of gravity,

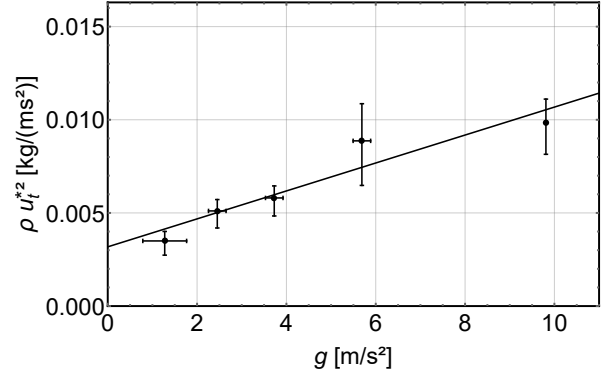


Figure 5: Dependence of the measured threshold shear stress on gravity g overlaid by the model of Shao and Lu (2000). The linear fit is described by $\rho u_t^{*2}(g) = (7.5 \pm 1.5) \times 10^{-4} \text{ kg m}^{-2} \cdot g + (3.2 \pm 0.8) \times 10^{-3} \text{ kg m}^{-1} \text{ s}^{-2}$.

while the surface energy γ is a measure of cohesion. A_N is a dimensionless coefficient.

The linear dependence of the threshold shear stress on gravity is in agreement with the experimental data as seen in Fig. 5. Assuming a mean particle size of $d = 100 \mu\text{m}$, the linear fit in Fig. 5 yields $A_N = (2.7 \pm 0.5) \times 10^{-3}$ and $\gamma = (1.2 \pm 0.5) \times 10^{-4} \text{ J/m}^2$. Again, the uncertainties are obtained by error propagation considering the error of the fit in Fig. 5. We note, that these values are calculated for monodisperse particles with $d = 100 \mu\text{m}$. As shown in Fig. 2, this is an approximation to our sample. Nonetheless, we consider the calculated values to be useful to give an estimate of the magnitude of A_N and γ . The fit also indicates that, for the given sample of irregular shaped MMS particles, cohesion plays an important role as it dominates over gravity below an acceleration of around 4 m s⁻². This behavior stands in contrast to the result of Demirci et al. (2019) who used glass beads of a much larger diameter. As expected, the reaction to wind exposure of that sample is mainly dominated by gravity.

3.2. Erosion Rates

In addition to the threshold wind velocities for motion initiation, also the erosion rates for stronger winds were measured. If $u_a^* > u_t^*$ grains are removed and the shape of the surface changes as Fig. 6 illustrates. Panels (a) and (b) show raw images of the samples with grains being lifted by the wind drag (panel (a) the start of the experiment and (b) the end of the experiment). To determine the eroded mass at a given time the initial image at time zero and the image at the given time are binarized and the difference image is calculated as shown in panel (c). The eroded material appears black

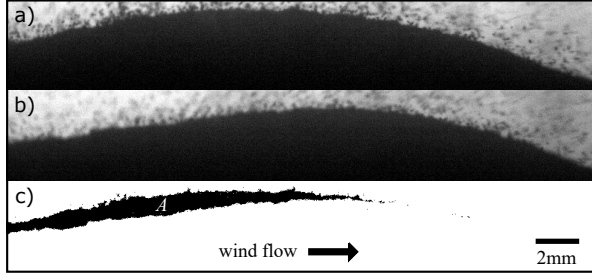


Figure 6: Erosion at the windward side with an applied wind velocity of $u_a^* = 1.03 \text{ m s}^{-1}$ and $g = 2.5 \text{ m s}^{-2}$. a) and b) show the shape of the surface at the beginning of the measurement and around 11s later while c) is the difference of both images. The size of the black area in c) is defined as A and displays the eroded material.

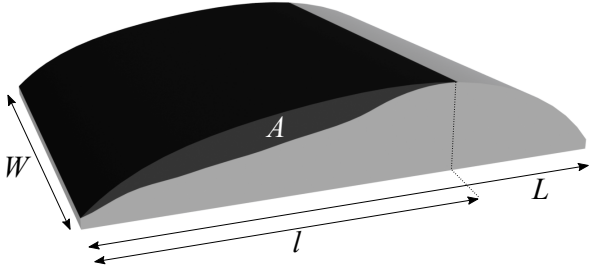


Figure 7: Schematic view of the assumed dimensions of the particle bed and the eroded area A which can be extracted from the image data. Here, the eroded volume is marked in dark gray.

in the difference image. The cross-sectional area A of this eroded material is used to quantify the erosion rate. As only the two-dimensional cross section is visible, the real 3D shape of the heap is not accessible for observation and its extent in the third dimension has to be estimated. Here, the particle bed is modeled as depicted in Fig. 7. While W and L describe the dimensions of the heap, l measures the extent of the heap where erosion is observed. For simplicity, in this model the eroded volume is assumed to be $V = A \cdot W$. We note that this is an overestimation as the real shape is not known and the cross section along W might be curved. The volume V can be converted to the eroded mass using the bulk density ρ of the sample which was measured on ground to $\rho = 1110 \text{ kg m}^{-3}$. The eroded mass alone is not a suitable quantity to compare different measurements. Due to the shutter of the sample bed, the heap cannot repeatedly be prepared in the same way and its size varies. To take that into account, the eroded mass is normalized to the active surface area where erosion is observed. This yields

$$M_{\text{norm}} = \frac{\rho \cdot V}{l \cdot W} = \frac{\rho \cdot A}{l}. \quad (4)$$

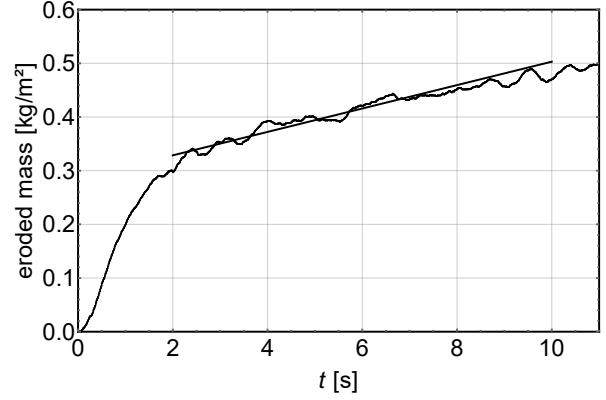


Figure 8: Evolution of the cumulative eroded mass normalized to the surface area where erosion is observed. The linear fit yields an erosion rate of $\epsilon \approx 0.02 \text{ kg m}^{-2} \text{ s}^{-1}$. The applied wind velocity was $u_a^* = 1.03 \text{ m s}^{-1}$ at an acceleration of $g = 2.5 \text{ m s}^{-2}$.

Fig. 8 shows the temporal evolution of the cumulated eroded mass during the measurement shown in Fig. 6. Once the shutter opens, a large amount of grains is entrained and settles back shortly after. During the first seconds, this loose layer is removed easily until the windward side is adapted to the wind exposure. Then, typical slope angles of the particle bed are around 6 to 10° in our experiments. This adaptation period is mirrored by the disequilibrium in Fig. 8. The number of saltating grains grows abruptly leading to a steep increase of the eroded mass until an equilibrium is established with linear mass loss. This is equivalent to a constant erosion rate ϵ . Slight variations of the eroded mass over time appear due to the accuracy of the binarization (see Fig. 6c). This analysis is not sensitive to particle size. The erosion process is not constrained to individual grains but whole layers of material are removed.

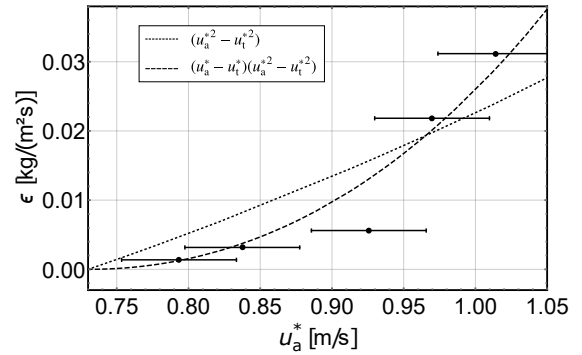


Figure 9: Erosion rates under Martian gravity ($u_t^* = 0.73 \text{ m s}^{-1}$) at various applied wind velocities.

At first, the erosion rate was studied under Martian conditions. The wind speeds were varied between the threshold value $u_t^* = 0.73 \text{ m s}^{-1}$ and the maximum speed. As expected, erosion gets stronger at larger wind speeds above the threshold, as seen in Fig. 9.

Recent models predict the erosion rate to be proportional to the excess shear stress $\epsilon \sim \tau_a - \tau_{cr}$ (Martin and Kok, 2017). The critical stress τ_{cr} is mostly associated to the impact or dynamical threshold, which is lower than the fluid threshold τ_t (Kok, 2010a). This quantity takes into account that the saltation process can be sustained by impacts of entrained particles (Durán et al., 2011). The impact threshold is not accessible in our experiment since the measurement time in one parabola is too short to change the wind speed during a parabola. Here, erosion can only be related to the fluid threshold. Creyssels et al. (2009) and Durán et al. (2011) find a quadratic dependence on the applied friction velocity in wind tunnel experiments. Fig. 9 includes a fit scaling linearly with the excess shear stress and thus quadratically with the applied friction velocity. Furthermore, the data is also fitted to a cubic dependence on the velocity as was proposed by Ho et al. (2011) for a rigid particle bed. Durán et al. (2011) also find a cubic scaling for velocities well above the threshold. It has to be noted that, here, the fluid threshold is used instead of the impact threshold.

By applying the analysis to measurements carried out under varying acceleration, it is possible to investigate the influence of gravity on the erosion rate. The applied wind velocity was set to the maximum value. The results are summarized in Fig. 10. The determined erosion rates are accurate to a percent level. The large variations are due to different particle bed conditions. Nevertheless, spanning an order of magnitude, the data show a clear decrease of erosion rate with gravity as expected. A trend line scaling linearly with gravity is included.

4. Discussion and Conclusion

The threshold friction velocity for wind induced motion of Mojave Mars Simulant grains was measured under Martian conditions. The values are even slightly lower than those obtained by Musiolik et al. (2018) for JSC sand of a comparable size distribution. Thus, the results presented here extend the range of materials which allow motion initiation at lower wind speeds than thought before. Simulations of sand transport on Mars could therefore rely on lower thresholds without artificially reducing these values.

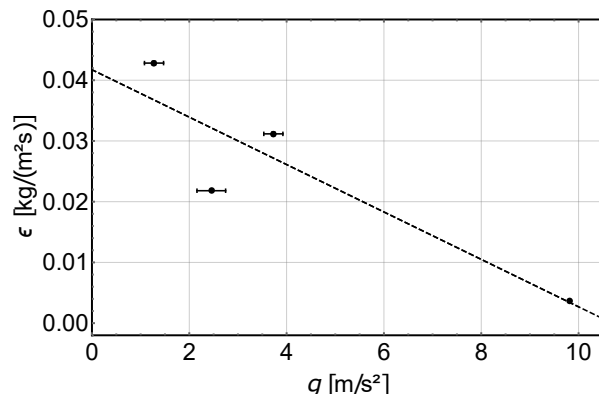


Figure 10: Erosion rates at fixed applied wind velocity $u_a^* = 1.03 \text{ m s}^{-1}$ and varying gravitational acceleration. The trend line scales linearly with gravity.

The general dependence between threshold shear stress and gravity below $1 g_E$ and for mbar pressure could be studied experimentally. For the given sample and in the mbar pressure regime the data can be explained by the theoretical model of Shao and Lu (2000). There are also several bodies in the Solar System showing wind phenomena. Of course, neither the chosen gas type and pressure nor the used sample material are representative for other planetary bodies than Mars. However, the results give an estimate of how particle motion is triggered on surfaces of exoplanets with lower gravity.

To understand particle transport and to make any predictions about weather phenomena on those bodies, it is also crucial to know erosion rates. The evaluation of the amount of eroded particles presented here is far from being exact due to the lack of 3D information and varying shapes of the particle bed. However, the eroded mass can be estimated by using the model presented in Fig. 7. A more thorough analysis of the erosion process would require a better measurement of the eroded mass as well as a longer observation time, which is a limited resource in parabolic flights. The residual acceleration of the aircraft and the need to lift the sample during the microgravity phase usually limit the observation time to less than 10 s.

The data are compared to two different models with quadratic and cubic dependence on u_a^* . As the impact threshold cannot be measured here, the models differ from those by Ho et al. (2011) and Martin and Kok (2017). According to the data the erosion rate seems to grow rather cubic-like under Martian conditions. Kok (2010a) found an impact threshold to maintain saltation which is an order of magnitude lower than the thresh-

old u_t^* to initiate the saltation process. This large difference cannot be confirmed by this experiment as the exact value for the impact threshold was not measured. Making a more accurate statement would require more and better measurements. The characteristics of the erosion process are not representative for all local Martian conditions, but our data may give an idea of the change of erosion with speed for shallow slopes.

Finally, the presented study is a first investigation of how erosion rates are influenced by lower gravity which has not been subject of experimental work so far.

Acknowledgements

The experiment was funded by DLR space administration under grants 50 WM 1542 and 50 WM 1760. We appreciate access to the parabolic flights which was granted by ESA. M. K. is supported by the DFG under grant WU 321/14-1.

References

References

Baker, M. M., Newman, C. E., Lapotre, M. G. A., Sullivan, R., Bridges, N. T., and Lewis, K. W. (2018). Coarse sediment transport in the modern martian environment. *Journal of Geophysical Research: Planets*, 123(6):1380–1394.

Bridges, N. T., Bourke, M. C., Geissler, P. E., Banks, M. E., Colon, C., Diniega, S., Golombek, M. P., Hansen, C. J., Mattson, S., McEwen, A. S., Mellon, M. T., Stantzos, N., and Thomson, B. J. (2012). Planet-wide sand motion on Mars. *Geology*, 40:31–34.

Creyssels, M., Dupont, P., El Moctar, A. O., Valance, A., Cantat, I., Jenkins, J. T., Pasini, J. M., and Rasmussen, K. R. (2009). Saltating particles in a turbulent boundary layer: experiment and theory. *Journal of Fluid Mechanics*, 625:47–74.

Daerden, F., Whiteway, J. A., Neary, L., Komguem, L., Lemmon, M. T., Heavens, N. G., Cantor, B. A., Hbrard, E., and Smith, M. D. (2015). A solar escalator on mars: Self-lifting of dust layers by radiative heating. *Geophysical Research Letters*, 42(18):7319–7326.

de Beule, C., Wurm, G., Kelling, T., Küpper, M., Jankowski, T., and Teiser, J. (2014). The martian soil as a planetary gas pump. *Nature Physics*, 10:17–20.

Demirci, T., Kruss, M., Teiser, J., Bogdan, T., Jungmann, F., Schneider, N., and Wurm, G. (2019). Are pebble pile planetesimals doomed? *Monthly Notices of the Royal Astronomical Society*, page stz107.

Durán, O., Claudin, P., and Andreotti, B. (2011). On aeolian transport: Grain-scale interactions, dynamical mechanisms and scaling laws. *Aeolian Research*, 3(3):243–270.

Ellehoj, M. D., Gunnlaugsson, H. P., Taylor, P. A., Kahanpää, H., Bean, K. M., Cantor, B. A., Gheyhani, B. T., Drube, L., Fisher, D., Harri, A. M., Holstein-Rathlou, C., Lemmon, M. T., Madsen, M. B., Malin, M. C., Polkko, J., Smith, P. H., Tamppari, L. K., Weng, W., and Whiteway, J. (2010). Convective vortices and dust devils at the Phoenix Mars mission landing site. *Journal of Geophysical Research (Planets)*, 115:E00E16.

exoplanet.eu (2019). The extrasolar planets encyclopaedia.

Forget, F., Hourdin, F., Fournier, R., Hourdin, C., Talagrand, O., Collins, M., Lewis, S. R., Read, P. L., and Huot, J.-P. (1999). Improved general circulation models of the martian atmosphere from the surface to above 80 km. *Journal of Geophysical Research: Planets*, 104(E10):24155–24175.

Goudie, A. and Middleton, N. (2001). Saharan dust storms: nature and consequences. *Earth-Science Reviews*, 56(1):179–204.

Goudie, A. S. and Middleton, N. J. (1992). The changing frequency of dust storms through time. *Climatic Change*, 20(3):197–225.

Greeley, R. and Iversen, J. D. (1985). Wind as a geological process on earth, mars, venus and titan. *New York: Cambridge University Press*.

Greeley, R., Leach, R., White, B., Iversen, J., and Pollack, J. (1980). Threshold windspeeds for sand on mars: Wind tunnel simulations. *Geophysical Research Letters*, 7(2):121–124.

Greeley, R., Whelley, P. L., Arvidson, R. E., Cabrol, N. A., Foley, D. J., Franklin, B. J., Geissler, P. G., Golombek, M. P., Kuzmin, R. O., Landis, G. A., Lemmon, M. T., Neakrase, L. D. V., Squyres, S. W., and Thompson, S. D. (2006). Active dust devils in gusev crater, mars: Observations from the mars exploration rover spirit. *Journal of Geophysical Research: Planets*, 111(E12).

Greeley, R., White, B., Leach, R., Iversen, J., and Pollack, J. (1976). Mars: Wind friction speeds for particle movement. *Geophysical Research Letters*, 3(8):417–420.

Heavens, N. G., Richardson, M. I., Kleinbhl, A., Kass, D. M., McCleese, D. J., Abdou, W., Benson, J. L., Schofield, J. T., Shirley, J. H., and Wolkenberg, P. M. (2011). Vertical distribution of dust in the martian atmosphere during northern spring and summer: High-altitude tropical dust maximum at northern summer solstice. *Journal of Geophysical Research: Planets*, 116(E1).

Hess, S. L., Henry, R. M., Leovy, C. B., Ryan, J. A., and Tillman, J. E. (1977). Meteorological results from the surface of mars: Viking 1 and 2. *Journal of Geophysical Research (1896-1977)*, 82(28):4559–4574.

Ho, T. D., Valance, A., Dupont, P., and Ould El Moctar, A. (2011). Scaling laws in aeolian sand transport. *Phys. Rev. Lett.*, 106:094501.

Holstein-Rathlou, C., Gunnlaugsson, H. P., Merrison, J. P., Bean, K. M., Cantor, B. A., Davis, J. A., Davy, R., Drake, N. B., Ellehoj, M. D., Goetz, W., Hviid, S. F., Lange, C. F., Larsen, S. E., Lemmon, M. T., Madsen, M. B., Malin, M., Moores, J. E., Nrnberg, P., Smith, P., Tamppari, L. K., and Taylor, P. A. (2010). Winds at the phoenix landing site. *Journal of Geophysical Research: Planets*, 115(E5).

Kok, J. F. (2010a). Difference in the wind speeds required for initiation versus continuation of sand transport on mars: Implications for dunes and dust storms. *Phys. Rev. Lett.*, 104:074502.

Kok, J. F. (2010b). An improved parameterization of wind-blown sand flux on mars that includes the effect of hysteresis. *Geophysical Research Letters*, 37(12).

Kok, J. F., Parteli, E. J. R., Michaels, T. I., and Karam, D. B. (2012). The physics of wind-blown sand and dust. *Reports on Progress in Physics*, 75(10):106901.

Laesecke, A. and Muzny, C. D. (2017). Reference correlation for the viscosity of carbon dioxide. *Journal of Physical and Chemical Reference Data*, 46(1):013107.

Lapotre, M. G. A., Ewing, R. C., Lamb, M. P., Fischer, W. W., Grotzinger, J. P., Rubin, D. M., Lewis, K. W., Ballard, M. J., Day, M., Gupta, S., Banham, S. G., Bridges, N. T., Des Marais, D. J., Fraeman, A. A., Grant, J. A., Herkenhoff, K. E., Ming, D. W., Mischna, M. A., Rice, M. S., Sumner, D. Y., Vasavada, A. R., and Yingst, R. A. (2016). Large wind ripples on mars: A record of atmospheric evolution. *Science*, 353(6294):55–58.

Martin, R. L. and Kok, J. F. (2017). Wind-invariant saltation heights imply linear scaling of aeolian saltation flux with shear stress. *Sci-*

- ence *Advances*, 3:e1602569.
- Merrison, J., Bechtold, H., Gunlaugsson, H., Jensen, A., Kinch, K., Nornberg, P., and Rasmussen, K. (2008). An environmental simulation wind tunnel for studying aeolian transport on mars. *Planetary and Space Science*, 56(3):426 – 437.
- Musioli, G., Kruss, M., Demirci, T., Schirnski, B., Teiser, J., Daerden, F., Smith, M. D., Neary, L., and Wurm, G. (2018). Saltation under martian gravity and its influence on the global dust distribution. *Icarus*, 306:25 – 31.
- Peters, G. H., Abbey, W., Bearman, G. H., Mungas, G. S., Smith, J. A., Anderson, R. C., Douglas, S., and Beegle, L. W. (2008). Mojave mars simulant - characterization of a new geologic mars analog. *Icarus*, 197(2):470 – 479.
- Rasmussen, K. R., Valance, A., and Merrison, J. (2015). Laboratory studies of aeolian sediment transport processes on planetary surfaces. *Geomorphology*, 244:74 – 94. Laboratory Experiments in Geomorphology 46th Annual Binghamton Geomorphology Symposium 18-20 September 2015.
- Schlichting, H. and Gersten, K. (2006). *Grenzschicht-Theorie*. Springer.
- Schofield, J. T., Barnes, J. R., Crisp, D., Haberle, R. M., Larsen, S., Magalhães, J. A., Murphy, J. R., Seiff, A., and Wilson, G. (1997). The mars pathfinder atmospheric structure investigation/meteorology (asi/met) experiment. *Science*, 278(5344):1752–1758.
- Schütz, L., Jaenicke, R., and Pietrek, H. (1981). Saharan dust transport over the North Atlantic Ocean. In *Desert Dust: Origin, Characteristics, and Effect on Man*. Geological Society of America.
- Shao, Y. and Lu, H. (2000). A simple expression for wind erosion threshold friction velocity. *Journal of Geophysical Research: Atmospheres*, 105(D17):22437–22443.
- Smith, M. D. (2004). Interannual variability in tes atmospheric observations of mars during 1999/2003. *Icarus*, 167(1):148 – 165. Special Issue on DSI/Comet Borrelly.
- Sternberg, J. (1962). A theory for the viscous sublayer of a turbulent flow. *Journal of Fluid Mechanics*, 13(2):241–271.
- Sullivan, R., Arvidson, R., Bell III, J. F., Gellert, R., Golombek, M., Greeley, R., Herkenhoff, K., Johnson, J., Thompson, S., Whelley, P., and Wray, J. (2008). Wind-driven particle mobility on mars: Insights from mars exploration rover observations at el dorado and surroundings at gusev crater. *Journal of Geophysical Research: Planets*, 113(E6).
- Sullivan, R., Banfield, D., Bell, J. F., Calvin, W., Fike, D., Golombek, M., Greeley, R., Grotzinger, J., Herkenhoff, K., Jerolmack, D., Malin, M., Ming, D., Soderblom, L. A., Squyres, S. W., Thompson, S., Watters, W. A., Weitz, C. M., and Yen, A. (2005). Aeolian processes at the Mars Exploration Rover Meridiani Planum landing site. *Nature*, 436:58–61.
- White, B., Greeley, R., Leach, R., and Iversen, J. (1987). Saltation threshold experiments conducted under reduced gravity conditions. *25th AIAA Aerospace Sciences Meeting*, page 621.
- Wurm, G., Blum, J., and Colwell, J. E. (2001). A new mechanism relevant to the formation of planetesimals in the solar nebula. *Icarus*, 151(2):318 – 321.
- Zurek, R. W. (2017). *Understanding Mars and Its Atmosphere*, page 3&19. Cambridge Planetary Science. Cambridge University Press.